

Article

Seismic Response and Security Assessment of Cross-Fault Hydraulic-Tunnel Lining Structures

Qingteng Yuan ^{1,2,*} , Ming Xiao ^{1,2}, Ci Kong ^{1,2}  and Kaicheng Wang ^{1,2}

¹ State Key Laboratory of Water Resources Engineering and Management, Wuhan University, Wuhan 430072, China; mxiao@whu.edu.cn (M.X.); 2015301580086@whu.edu.cn (C.K.); wkczlh@whu.edu.cn (K.W.)

² Key Laboratory of Rock Mechanics in Hydraulic Structural Engineering of Ministry of Education, Wuhan University, Wuhan 430072, China

* Correspondence: 2015301580066@whu.edu.cn

Abstract: The foundation of a seismic safety assessment of cross-fault hydraulic tunnels is an acceptable and accurate seismic response. A dynamic contact force algorithm that may take into consideration the interaction between the fault-surrounding rock-lining structure was devised in light of the contact characteristics of various media in cross-fault hydraulic tunnels under seismic activity. A quantitative instability criterion using a relative displacement ratio as the criterion was devised based on the cusp catastrophe model. By using the cross-fault hydraulic tunnel of the Lawa Hydropower Station as an example, it was possible to evaluate and assess the impacts of four working circumstances on the seismic response of the tunnel lining structure. The findings demonstrated that the lining haunch exhibited stronger stress and displacement responses when subjected to seismic activity. The consideration of fault-surrounding rock-lining interaction exacerbated the displacement and stress seismic responses of the lining structure. The haunch, bottom arch, and top arch of the lining's characteristic parts—which ranged in size from large to small—responded more seismically as peak ground acceleration rose. Applying the aforementioned instability criterion, the haunch, bottom arch, and top arch of the liner structure could withstand maximum peak ground accelerations of 0.10 g, 0.20 g, and 0.35 g, respectively. The aforementioned technique offers a fresh perspective on how to evaluate the seismic response and seismic safety of the tunnel's lining structure, and the study's findings can serve as a guide for seismic design.

Keywords: hydraulic tunnel; seismic response; dynamic contact force algorithm; lining structure; cusp catastrophe model; safety assessment



Citation: Yuan, Q.; Xiao, M.; Kong, C.; Wang, K. Seismic Response and Security Assessment of Cross-Fault Hydraulic-Tunnel Lining Structures. *Buildings* **2023**, *13*, 2348. <https://doi.org/10.3390/buildings13092348>

Academic Editor: Suraparb Keawsawasvong

Received: 17 July 2023

Revised: 9 September 2023

Accepted: 9 September 2023

Published: 15 September 2023



Copyright: © 2023 by the authors. Licensee MDPI, Basel, Switzerland. This article is an open access article distributed under the terms and conditions of the Creative Commons Attribution (CC BY) license (<https://creativecommons.org/licenses/by/4.0/>).

1. Introduction

Hydraulic tunnels are an important part of water diversion and transfer projects and are the lifeline of cross-regional water resource dispatch. Due to their long-distance water transmission, they are inevitably located in high-intensity seismic regions and inevitably traverse fault fracture zones. It has been shown that underground structures such as tunnels, pipelines, and metro stations also suffer severe damage under seismic action [1–8]. It is evident that hydraulic tunnels located in high-intensity seismic regions may face serious seismic problems. Relevant studies and seismic-damage investigations [9–12] have shown that the crossing of fault fracture zones is a weak point in the seismic design of hydraulic-tunnel lining structures. Therefore, it is of great significance to study the seismic response of cross-fault hydraulic tunnels and their seismic safety in order to ensure the safe operation of these projects.

Research on the seismic response of hydraulic tunnels has been fruitful. Peng et al. [13] investigated the seismic dynamic response and the sensitivity of the response of tunnels traversing faults using numerical simulations. Chen et al. [14] considered the frictional contact surface between the fault and the surrounding rock and investigated the changes in

displacement, strain, and maximum principal stress of the lining under the influence of the fault by numerical methods. Li et al. [15] used a combination of structural surface elements and solid elements to simulate faults and studied the dynamic response characteristics of cross-fault tunnels. Wang et al. [16] used a nonlinear thin-layer element to simulate the mechanical characteristics of faults and analyzed the effects of fault thickness, dip, and peak ground-shaking acceleration on the seismic response of the surrounding rocks in underground caverns. Liu et al. [17,18] established a dynamic contact force algorithm that can consider multiple contact states between the fault and the surrounding rock and found that the stress and displacement of the lining structure increased uniformly after considering the contact between the surrounding rock and the fault. Shahidi et al. [19] investigated the longitudinal seismic response of tunnels using numerical methods and proposed a design method for flexible lining structures across faults. Huang et al. [11] investigated the nonlinear seismic response of hydraulic tunnels across faults under the action of obliquely incident P-waves. Liu et al. [20] investigated the effect of initial support on the seismic response of the lining under seismic action. Zlatanović et al. [21] investigated the interaction between soil and tunnel structure under seismic action in different soil conditions based on the commercial software ANSYS. Wang et al. [22] and Liu et al. [23] established a joint bearing analysis model of the surrounding rock and lining and studied the seismic response characteristics of the inlet section of the tunnel. The current research mainly focused on the simulation of fault and fault–rock interaction alone, or the simulation of the interaction between the surrounding rock and the lining structure alone. However, a cross-fault hydraulic tunnel is a system consisting of faults, surrounding rocks, and lining structures, and the simulation of the interaction between the two materials alone cannot accurately simulate the seismic response of the tunnel. Therefore, the establishment of a suitable fault–surrounding rock–lining structure interaction model is crucial to accurately simulating the seismic response of cross-fault hydraulic tunnels.

At present, the commonly used criteria for judging the instability of underground caverns in seismic dynamic analysis include the displacement of key monitoring points increasing from slow to fast, and the plastic deformation of surrounding rock being large, resulting in the calculation not converging. These criteria are qualitative judging methods [24]. In addition, Kumar et al. [25,26] proposed non-dimensional stability numbers for evaluating the stability of unsupported circular tunnels under seismic loading; Liu et al. [27] proposed a dynamic analysis method for seismic-stability evaluation of underground tunnels based on deformation reinforcement theory; and Cheng et al. [28] investigated the effect of the dynamic parameters of the soil body on the factor of safety as a criterion for evaluating the seismic stability of tunnels. Existing research methods have some limitations. The cusp mutation model has been more often used in geotechnical disasters such as landslides [29–31], rock bursts [32,33], and water inrush and mud inrush [34,35], for describing and explaining the phenomena of discontinuities and jumps in them. Du et al. [36] established a cusp mutation model that can simultaneously take into account both the weakening and hardening of slip zones and revealed the triggering mechanism of landslide instability. Earthquakes are similar to rock bursts, etc., with discontinuities and sudden jumps, so they can also be explained by the cusp mutation model, but, at present, the cusp mutation model has been used less in earthquakes. Therefore, it is of great significance to establish a reasonable quantitative instability discrimination method based on the cusp mutation theory.

As a complex system of fault–surrounding rock–lining interactions, it is not comprehensive enough to consider only the influence of faults on the seismic response of hydraulic tunnels. Therefore, this paper establishes a joint bearing analysis model of fault–surrounding rock–lining interaction based on the dynamic contact force algorithm according to the characteristics of the interaction of the three types of media: surrounding rock, lining, and fault. The paper also establishes a quantitative instability criterion based on the cusp mutation model with the relative displacement ratio as the discriminant index. Taking the cross-fault hydraulic tunnel of Lawa Hydropower Station as an engineering

example, the seismic response characteristics of the tunnel lining structure were analyzed under the four working conditions of no interaction, surrounding rock–lining interaction, surrounding rock–fault interaction, and fault–rock–lining interaction, and the maximum peak acceleration that can be carried by the haunch, the bottom arch, and the top arch of the lining structure under the condition of surrounding rock–lining–fault interaction were investigated in order to provide a reference for the seismic design of the cross-fault hydraulic tunnels.

2. Fault–Surrounding Rock–Lining Structure Dynamic Analysis Model

Cross-fault hydraulic tunnels are complex systems composed of three different media: surrounding rock, fault, and lining structure. There are differences in the physical and mechanical properties of different media, and there are discontinuous contact surfaces between different media. Under the action of an earthquake, the seismic response of different media is different, which means that the lining and other media have relative displacements, which may lead to slip or separation of the lining and the surrounding rock, exacerbate the seismic response of the lining, and cause damage and cracking of the lining, which brings serious harm to the project. Therefore, it is of great significance to establish a suitable dynamic contact model that can reflect the interaction between multiple media. In this paper, based on the display integral algorithm of finite elements, the power contact joint bearing analysis model of a fault–surrounding rock–lining structure was established by comprehensively considering the contact conditions between different media.

2.1. Basic Finite Element Equations for Dynamic Contact Force Algorithms

Taking the contact model of the surrounding rock and lining structure as an example, as shown in Figure 1, the contact system is discretized by finite elements, and the discretized meshes on the contact surfaces of different media are the same, generating one-to-one corresponding node pairs, and the dynamic contact forces on the node pairs are equal in magnitude and opposite in direction [37,38]. The differential equation of motion for a node in a node pair is:

$$M\ddot{u} + C\dot{u} + Ku = P + N + T \quad (1)$$

where M is the contact node mass matrix, C is the contact node damping matrix, K is the contact node stiffness matrix, \ddot{u} is the contact node acceleration vector, \dot{u} is the contact node velocity vector, u is the contact node displacement vector, P is an external load, N is the normal vector of dynamic contact forces at the contact surface, and T is the tangential vector of dynamic contact forces at the contact surface.

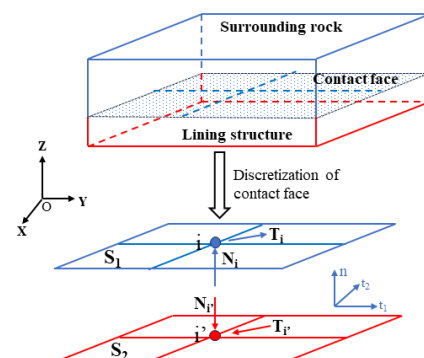


Figure 1. Contact system and dynamic contact force on contact face (adapted from [39]).

Discretizing the acceleration and velocity in Equation (1) using the central difference method yields:

$$\dot{u}^t = (u^{t+\Delta t} - u^{t-\Delta t}) / (2\Delta t) \quad (2)$$

$$\ddot{u}^t = (u^{t+\Delta t} - 2u^t + u^{t-\Delta t}) / \Delta t^2 \quad (3)$$

where Δt is time step.

Combining Equations (2) and (3) yields:

$$\ddot{u}^t = 2(u^{t+\Delta t} - u^t - \Delta t \dot{u}^t) / \Delta t^2 \quad (4)$$

Substituting Equation (4) into Equation (1) gives the expression at the $t + \Delta t$ time:

$$u^{t+\Delta t} = \bar{u}^{t+\Delta t} + \Delta t^2 M^{-1} (N^t + T^t) / 2 \quad (5)$$

$$\bar{u}^{t+\Delta t} = u^t + \Delta t \dot{u}^t + \Delta t^2 M^{-1} (-K^t u - C^t \dot{u} + P^t) / 2 \quad (6)$$

where $\bar{u}^{t+\Delta t}$ is the nodal displacement vector without consideration of dynamic contact forces.

Based on the basic assumptions of Newmark's long average acceleration method, the expressions for the velocity and acceleration of the contact node at the $t + \Delta t$ moment of contact are obtained as follows:

$$\dot{u}^{t+\Delta t} = 2(u^{t+\Delta t} - u^t) / \Delta t - \dot{u}^t \quad (7)$$

$$\ddot{u}^{t+\Delta t} = 2(\dot{u}^{t+\Delta t} - \dot{u}^t) / \Delta t - \ddot{u}^t \quad (8)$$

At the t time, the operational state of the contact nodes is known, but the dynamic contact force normal and tangential vectors (N^t and T^t) are not known. Therefore, the key to obtaining the state of motion of the contact node at the $t + \Delta t$ moment of contact is to solve for the unknown quantities at the moment of contact N^t and T^t .

2.2. Solving for Dynamic Contact Forces Considering Multiple Contact States

The key idea in solving for the dynamic contact forces on the contact surface is to make assumptions plus corrections: first assume that the node pairs on the contact surface are in adhesive contact and satisfy the deformation coordination conditions, and then correct the calculated dynamic contact forces according to the mechanical constraints.

Assuming that there is no slip on the contact surface at the $t + \Delta t$ moment, any node pair i and i' satisfies the condition of no mutual embeddedness in the normal direction and no relative slip in the tangential direction:

$$n_i^S (u_{i'}^{t+\Delta t} - u_i^{t+\Delta t}) = 0 \quad (9)$$

$$\tau_i^S (u_{i'}^{t+\Delta t} - u_i^{t+\Delta t}) = \tau_i^S (u_{i'}^t - u_i^t) \quad (10)$$

where n_i is the unit normal vector of the contact node pair, the positive direction is the node direction i to τ_i , and is the corresponding unit tangential vector.

Let $\Delta_{1i} = n_i^S (\bar{u}_{i'}^{t+\Delta t} - \bar{u}_i^{t+\Delta t})$, substitute Equation (5) into Equation (9):

$$\Delta_{1i} = n_i^S [\Delta t^2 M_i^{-1} (N_i^t + T_i^t) / 2 - \Delta t^2 M^{-1} (N_{i'}^t + T_{i'}^t) / 2] \quad (11)$$

Let $\Delta_{2i} = \tau_i^S [\bar{u}_{i'}^{t+\Delta t} - \bar{u}_i^{t+\Delta t} - (u_{i'}^t - u_i^t)]$ substitute Equation (5) into Equation (10):

$$\Delta_{2i} = \tau_i^S [\Delta t^2 M_i^{-1} (N_i^t + T_i^t) / 2 - \Delta t^2 M_{i'}^{-1} (N_{i'}^t + T_{i'}^t) / 2] \quad (12)$$

The normal and tangential dynamic contact force vectors at the two nodes in a node pair at the t moment satisfy the relationship:

$$\begin{aligned} N_i^t + N_{i'}^t &= 0 \\ T_i^t + T_{i'}^t &= 0 \end{aligned} \quad (13)$$

Knowing that $n_i^T T_i^t = 0$ and $\tau_i^T N_i^t = 0$, we have from Equations (11) and (12), respectively, that:

$$N_i^t = \frac{2M_i M_{i'}}{(M_i + M_{i'}) \Delta t^2} (\bar{u}_{i'}^{t+\Delta t} - \bar{u}_i^{t+\Delta t}) \quad (14)$$

$$T_i^t = \frac{2M_i M_{i'}}{(M_i + M_{i'}) \Delta t^2} [\bar{u}_{i'}^{t+\Delta t} - \bar{u}_i^{t+\Delta t} - (u_{i'}^t - u_i^t)] \quad (15)$$

The dynamic contact forces obtained in Equations (14) and (15) are obtained by solving for different media in cohesive contact. Under seismic loading, there are various contact states between different media, such as adhesion, slip, and disengagement, so the dynamic contact force needs to be corrected.

Damage to the contact surface is mainly caused by normal cracking and tangential slip. The tensile strength of the contact surface is low, and therefore the contact surface tensile stress calibration should have a higher priority. Equation (16) calibrates the contact condition in the normal and tangential directions and corrects for contact forces.

$$\begin{aligned} N_i^t = T_i^t = 0 & \quad (n_i^T \cdot N_i^t > 0 \cap \|N_i^t\| > \sigma_t A_i) \\ T_i^t = 0 & \quad (n_i^T \cdot N_i^t > 0 \cap \|N_i^t\| \leq \sigma_t A_i) \\ T_i^t = \mu_d \|T_i^t\| \|N_i^t\| / \|T_i^t\| & \quad (n_i^T \cdot N_i^t \leq 0 \cap \|T_i^t\| > \mu_s \|N_i^t\| + c A_i) \end{aligned} \quad (16)$$

where μ_s and μ_d are the coefficients of static and dynamic friction of the contact surface, c and σ_t are the cohesive and tensile strengths of the contact surface, A_i are the control areas of the nodes i , $n_i^T \cdot N_i^t > 0$ indicates that the contact surface is in tension, $n_i^T \cdot N_i^t \leq 0$ indicates that the contact surface is in compression, and \cap indicates the intersection.

Unlike the contact of two media, the contact of three media may have contact surfaces that intersect. For the parts where the contact surfaces intersect, the idea of decomposition before superposition is used. Consider the contact between the three media of perimeter rock–lining–fault as an example. Breaking it down into perimeter rock–lining contact and perimeter rock–fault contact, use the method mentioned above to solve for the dynamic contact forces of each contact surface separately. Then, superimpose the dynamic contact forces of the intersecting nodes in a vector.

2.3. Basic Steps for the Implementation of the Dynamic Contact Force Algorithm

Prior to applying seismic stresses, one-to-one pairs of contact nodes are first set up between various media to achieve discontinuity in the finite element model, based on the node separation technique [40]. During seismic loading, some of the contact nodes may break through the cohesive forces and enter a sliding state, when it is necessary to identify the elements and their cell faces that are in contact with each other through a contact search.

General steps at $t + \Delta t$ moment for the display of finite element calculations for time-dependent multi-media dynamic contact systems:

- (a) The displacements of all contact nodes on different contact surfaces are calculated separately from Equation (6) without considering the dynamic contact forces;
- (b) Calculate the contact gap Δ_{1i} and Δ_{2i} , and from Equations (14) and (15), the dynamic contact force N_i^t and T_i^t ;
- (c) Discriminate the contact state and correct the dynamic contact forces; if there are intersecting contact surfaces, the dynamic contact forces of the intersecting contact nodes are superimposed vectorially;
- (d) Calculate the additional displacement field from Equation $\Delta u^{t+\Delta t} = \Delta t^2 M^{-1} (N^t + T^t) / 2$ and calculate the total displacement $u^{t+\Delta t}$ of the contact nodes from Equation (5);
- (e) Update model geometry information.

3. Safety Assessment Methods Based on Cusp Mutation Theory

3.1. Overview of Mutation Theory

Mutation theory is the study of various mutational phenomena using topology, bifurcation theory, singularity theory, and the concept of structural stability as a starting point. It describes in mathematical theory the phenomenon of sudden changes in the state of a system from a continuous change to a sudden jump to another state when external control variables occur. The advantage of mutation theory is that, even when the equations of a non-linear system are unknown, it is possible to determine and predict the qualitative or quantitative conditions under which a system will mutate based on only a few assumptions and using only a few control variables. Of the many primary mutation models, the cusp mutation model is the most widely used because of its simple functional form and clear physical meaning.

Zeeman [41] proposed the cusp mutation model in the 1970s with a potential function consisting of two control variables u and v and a state variable x , which can be expressed as:

$$V = \frac{1}{4}x^4 + \frac{u}{2}x^2 + vx \quad (17)$$

The corresponding equation for the equilibrium surface is:

$$\frac{\partial V}{\partial x} = x^3 + ux + v \quad (18)$$

It is a three-dimensional continuous surface with internal folding in the three-dimensional coordinate system, including the upper, middle, and lower lobes, as shown in Figure 2. The position of the equilibrium point in the middle lobe is the location of the extreme value of the potential function V , which is difficult to exist according to the principle of minimum potential energy for system stability, so the middle lobe is again the unreachable region of the potential function. The equilibrium point in the upper and lower lobes is the location of the minima of the potential function, whose equilibrium state is stable. Thus, the potential function mutation occurs at the locations where jumps occur in the upper and lower lobes, i.e., at the boundary lines of the middle lobe. When the equilibrium point jumps abruptly from the boundary of the upper lobe to the lower lobe or from the boundary of the lower lobe to the upper lobe at these junctions, the system is considered to have undergone a sudden change. These points, which lie on the boundary, satisfy the equation:

$$\frac{\partial^2 V}{\partial x^2} = 3x^2 + u = 0 \quad (19)$$

The points on the dividing line are referred to as the set of bifurcations. Combining Equations (18) and (19) and eliminating the state variables x , gives the expression after their projection on the control variable plane $u - v$:

$$4u^3 + 27v^2 = 0 \quad (20)$$

The bifurcation set divides the system into two regions. Points outside the bifurcation set region must be located in the upper or lower lobes and be in a stable state, and points within the bifurcation set region may be located in the upper, middle, and lower lobes. There are three equilibria, one of which is an unstable equilibrium. When the equilibrium point of the system crosses the bifurcation set and jumps between the upper and lower lobes, the system undergoes a mutation. The relationship between the state of the system and the bifurcation set can be expressed in terms of the mutation eigenvalues D :

$$D = 4u^3 + 27v^2 \quad (21)$$

When $D > 0$, the system is stable and does not mutate; when $D \leq 0$, the system may mutate across the bifurcation set and lose stability.

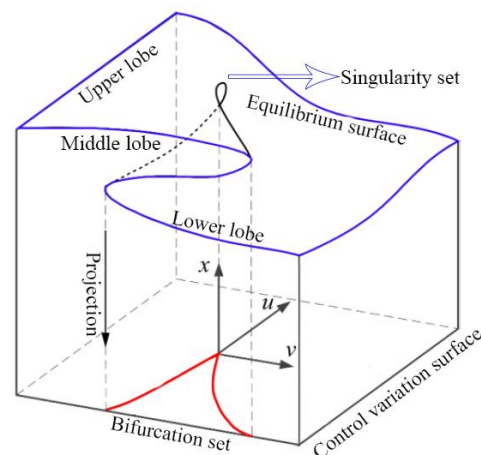


Figure 2. Space diagram of equilibrium surface of cusp catastrophe model (adapted from [32]).

3.2. Relative Displacement Ratio Mutation Criterion in Dynamic Analysis

Research [42] has shown that in structural dynamic analysis, the damage, strength, and stiffness of a structure are all related to its displacement, which can reflect the degradation of its strength and stiffness more comprehensively. There is a one-to-one correspondence with the state of seismic damage, and displacement is the easiest monitoring data to obtain in real earthquakes or model experiments. From a fine viewpoint, the different spatial locations of different parts of the lining structure result in differences in their overall fluctuating displacements, i.e., there are relative displacements. The criterion commonly used in dynamic analysis to determine the instability of underground chambers consists of a slow growth to a rapid increase in displacement at key monitoring points, which has a strong subjective element. Therefore, this study uses the post-earthquake relative displacement ratio of monitoring points as the state variable to study the critical state of instability occurring in the lining structure based on the theory of abrupt change at the cusp. In practical calculations, the basic idea of solving for the relative displacement ratio of the lining structure is as follows: selection of representative monitoring points at the location of the typical section of the model facing the void and reference points at the base of the model and calculation of the displacement difference between the monitoring point and the reference point in three directions Δu_x , Δu_y , and Δu_z . The total relative displacement can be calculated from Equation (22):

$$\Delta u = \sqrt{\Delta u_x^2 + \Delta u_y^2 + \Delta u_z^2} \quad (22)$$

The ratio of the relative displacement Δu to the tunnel span L is defined as the relative displacement ratio ω :

$$\omega = \frac{\Delta u}{L} \quad (23)$$

In geotechnical engineering, due to its complexity, the abrupt potential function for its structural stability is generally solved using inversion. To investigate the maximum peak seismic acceleration that the lining structure can withstand, a sudden change criterion was developed regarding the relationship between the relative displacement ratio of the monitoring points and the peak ground acceleration (PGA) function. The first step is to establish the relationship between the relative displacement ratio D_p at the monitoring point and the peak ground acceleration (PGA), convert it into a standardized function of the tip mutation model, calculate the eigenvalues of the mutation, calculate the peak acceleration of the mutation according to the conditions of the mutation, and determine the maximum peak acceleration that the lining structure can withstand. The specific steps are as follows:

The relationship between the lining structure monitoring points and the PGA is a series of continuously increasing functions $D_p(PGA)$. The polynomial function $D_p(t)$ is obtained by fitting the polynomial $D_p(PGA)$ with a 4th-order polynomial using the least-squares method, t is the peak acceleration. $D_p(t)$ can be expressed as:

$$D_p(t) = a_1 + a_2t + a_3t^2 + a_4t^3 + a_5t^4 \quad (24)$$

According to the Tschirnhaus variation, let $t = x - n$ and $n = a_4/4a_5$, be substituted in Equation (24) to eliminate the cubic term of t to obtain the following expression:

$$D_p(t) = b_1 + b_2r + b_3r^2 + b_4r^4 \quad (25)$$

$$\begin{bmatrix} b_1 \\ b_2 \\ b_3 \\ b_4 \end{bmatrix} = \begin{bmatrix} 1 & -n & n^2 & -n^3 & n^4 \\ 0 & 1 & -2n & 3n^2 & -4n^3 \\ 0 & 0 & 1 & -3n & 6n^2 \\ 0 & 0 & 0 & 0 & 1 \end{bmatrix} \begin{bmatrix} a_1 \\ a_2 \\ a_3 \\ a_4 \\ a_5 \end{bmatrix} \quad (26)$$

Dividing both sides of Equation (25) by $4b_4$ and omitting the constant term that has no effect on the eigenvalues of the mutation yields the transformed cusp mutation model:

$$V(x) = \frac{1}{4}x^4 + \frac{1}{2}ux^2 + vx \quad (27)$$

$$x = \frac{a_4}{4a_5} + t$$

$$u = \frac{b_3}{2b_4} \quad (28)$$

$$v = \frac{b_2}{4b_4}$$

where $V(x)$ is the potential function, x is the state variable, and u and v are the control variables.

Based on mutation theory, the mutation eigenvalues D can be calculated as:

$$D = 4u^3 + 27v^2 \quad (29)$$

The sudden change criteria regarding the relationship between the relative displacement ratio of the monitoring points and the peak acceleration function are all rigorously derived using mathematical formulas to quantify the criteria for the occurrence of instability and to be able to obtain the maximum peak acceleration that the lining structure can withstand at different inspection sites.

4. Example Analysis

4.1. Calculation Models and Parameters

The inlet section of the Lawa Hydropower Station is located in southwestern China, a region with complex geological conditions where the diversion tunnel passes through a number of developing faults. According to the research results, the basic seismic intensity of the area is VIII. The peak horizontal ground acceleration selected for the seismic response analysis in this study was 0.3 g. In order to study the seismic response and safety assessment of hydraulic tunnels across faults, a 3D finite element model, as shown in Figure 3, was established based on this project. The horizontal direction perpendicular to the cave axis was the X-axis, the horizontal direction parallel to the cave axis was the Y-axis, and the vertical direction was the Z-axis. The finite element model ranged from -60.0 to 60.0 m for 120.0 m in the X direction, -85.0 to 85.0 m for 170.0 m in the Y direction, and -60.0 to 60.0 m for 120.0 m in the Z direction. The diameter of the tunnel was 10.0 m, the thickness of the lining was 0.6 m, and it was cast in C30 reinforced concrete with a top burial depth of 55.0 m. The model was discretized using 6-sided 8-node elements, with 125,984 elements and 132,111 nodes divided, including 8928 lining elements. The maximum grid size was

no more than 5 m to meet the accuracy requirements of the dynamic time history method of calculation. The model contained a total of three materials: the surrounding rock, the fault, and the lining, and the relevant physical and mechanical parameters were as shown in Table 1. The cohesive force of each contact surface was assumed to be the average value of the cohesive force of the material on both sides of it, and the coefficient of static and dynamic friction of each contact surface was taken as 0.5.

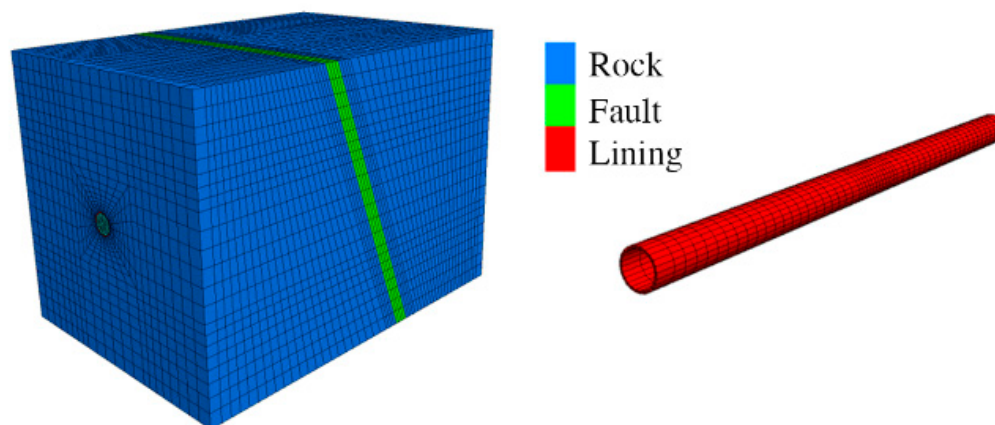


Figure 3. Three-dimensional finite element model.

Table 1. Physical and mechanical parameters of materials.

Materials	Density (g/cm ⁻³)	Elastic Modulus (GPa)	Poisson Ratio	Internal Friction Angle (°)	Cohesion (MPa)	Tensile Strength (MPa)	Compressive Strength (MPa)
Surrounding rock	2.7	6.5	0.280	43.50	0.95	2.00	30
Lining	2.5	30	0.167	42.00	1.75	1.43	15
Fault	2.3	1.0	0.400	19.29	0.07	0.60	10

4.2. The Calculation Process

In order to accurately simulate the tunnel construction and seismic response processes, the numerical simulation was divided into three parts: initial ground stress field inversion, static excavation, and dynamic response. By analyzing the test results of the ground stress measurement points, it was decided to use a gravity field with lateral pressure coefficients of $k_x = 1.4$, $k_y = 1.2$, and $k_z = 1.2$, as the initial ground stress field for the static calculations. The stress field from the excavation support calculation was used as the initial ground stress field for the dynamic time calculation. The dynamic calculation used the group's self-developed dynamic numerical calculation and analysis platform and embedded the dynamic contact force algorithm of the surrounding rock–fault–lining multi-material proposed in this study. An elastic-plastic damage intrinsic model [43] was used for the surrounding rock, faults, and concrete. The model had viscoelastic artificial boundaries on the top and bottom surfaces and free-field artificial boundaries on the four sides. The seismic waves were selected for the first 20 s of the EI-centro wave and were inputted vertically from the bottom of the model by amplitude modulation, filtering, and baseline correction. The calculation considered both x- and z-directional seismic wave excitations. The x-directional ground vibration acceleration time curve is shown in Figure 4, with a peak acceleration of 2.94 m/s², and the z-directional seismic wave was 2/3 of the x-directional seismic wave.

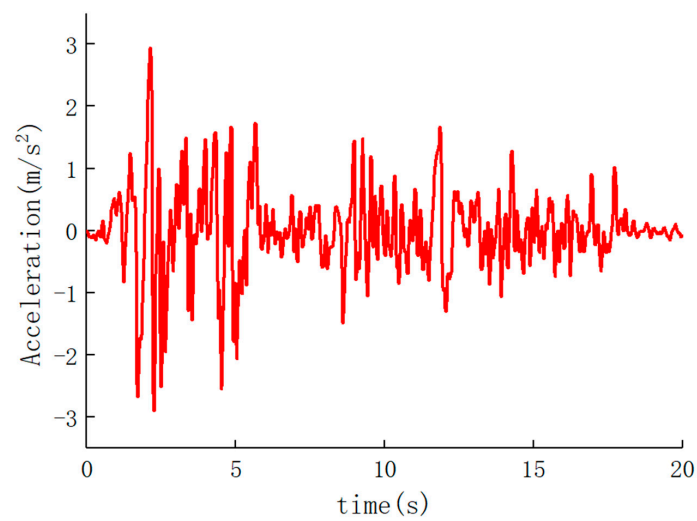
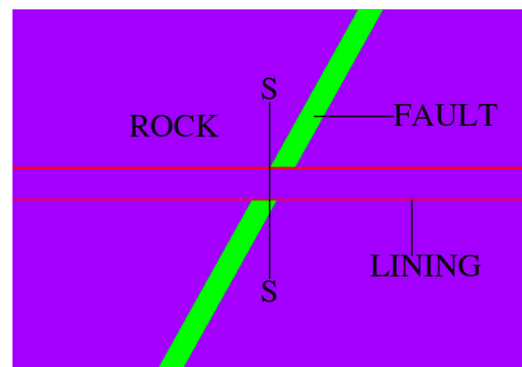


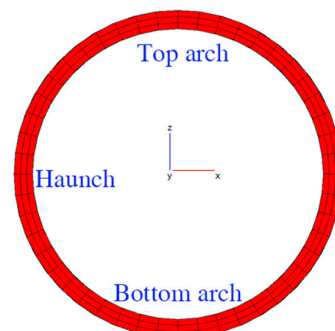
Figure 4. X-directional seismic wave acceleration–time curve.

5. Results and Discussion

To study the seismic response characteristics of different parts of the tunnel, a typical section and monitoring points were set up as shown in Figure 5, with a fault crossing at the typical section and monitoring points located at the top arch, bottom arch, and haunch of the lining structure at the typical section. In addition, a total of four calculation conditions were set up, as shown in Table 2.



(a) Typical section monitoring locations



(b) Distribution of monitoring sites

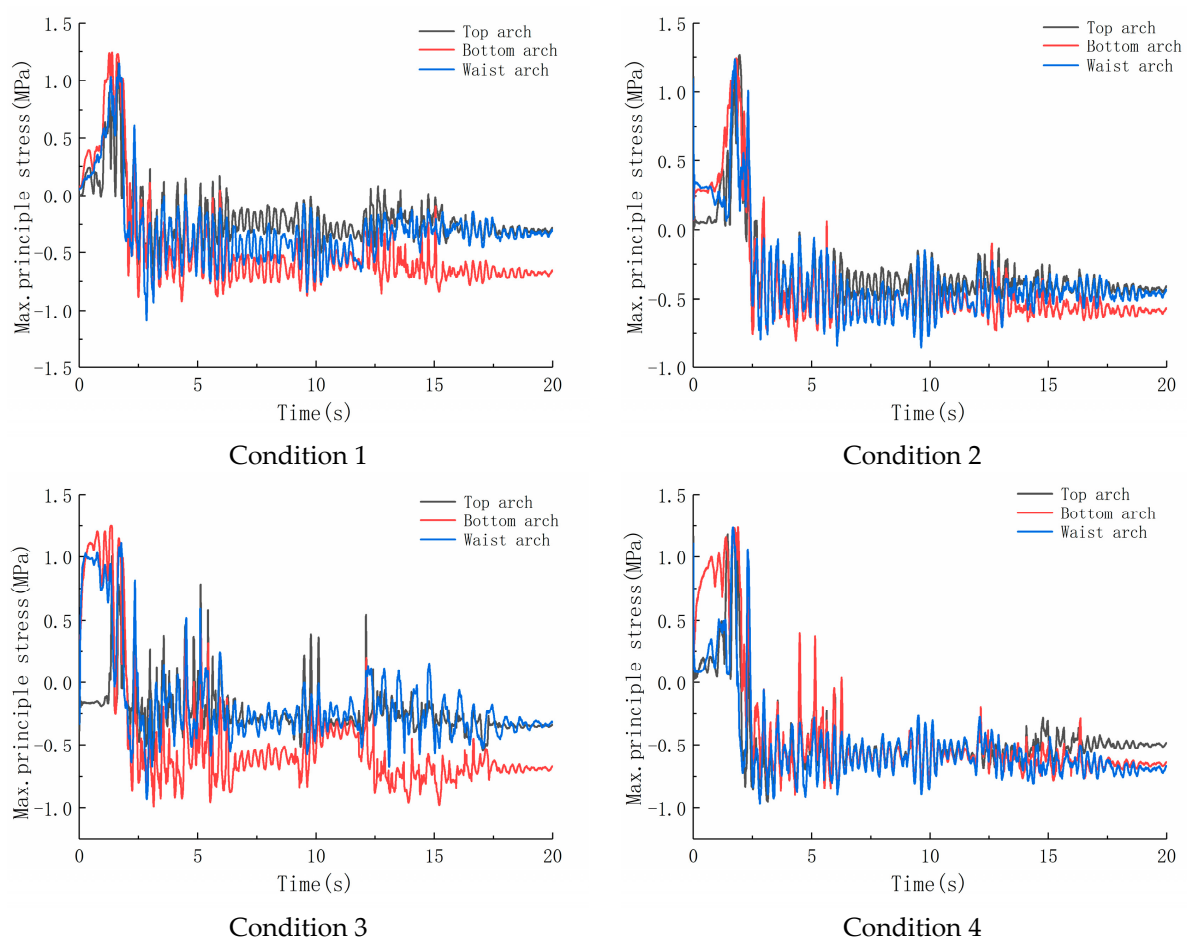
Figure 5. Monitoring schemes.

Table 2. Calculation of working conditions.

	Description
Condition 1	No interaction
Condition 2	Surrounding rock–lining interaction
Condition 3	Surrounding rock–fault interaction
Condition 4	Fault–surrounding rock–lining interaction

5.1. Stress Response Analysis of the Lining Structure

In view of the fact that the compressive strength of concrete materials is much greater than the tensile strength, tensile damage is the most common form of damage, so this study mainly analysed the variation of the maximum principal stress of the lining structure under different working conditions. The time course of the maximum principal stresses at the lining monitoring points for the four working conditions is shown in Figure 6. The maximum principal stress time curves for the top arch, bottom arch, and haunch of the lining under the four working conditions were similar in pattern, with the curves fluctuating sharply in the time period from 0 to 3.0 s, with smaller fluctuations in the time period from 3.0 to 7.0 s, and flattening out in the region after 7.0 s. The pattern of maximum principal stress fluctuations at each monitoring point was similar to the pattern of the input seismic wave acceleration time curve.

**Figure 6.** Maximum principal stress–time history of monitoring points of lining.

The maximum peak principal stress at each monitoring point under different working conditions is shown in Figure 7. The maximum peak principal stress in the bottom arch was basically unchanged under each working condition, with a value of about 1.24 MPa. The maximum principal stress peak in the top arch at condition 1 was 1.0 MPa; compared

to condition 1, the maximum principal stress peak in the top arch at conditions 2, 3, and 4 increased by 0.22 MPa, 0.15 MPa, and 0.27 MPa, respectively. The maximum peak principal stress in the girdle arch at condition 1 was 1.12 MPa. Compared to condition 1, the maximum peak principal stress in the girdle arch at Conditions 2, 3, and 4 increased by 0.12 MPa, 0.03 MPa, and 0.12 MPa, respectively. Comparing the four working conditions, it can be seen that the contact of different materials will aggravate the seismic response of the lining structure and increase the maximum principal stress peak, which is more likely to cause lining cracking damage and affect its normal operation.

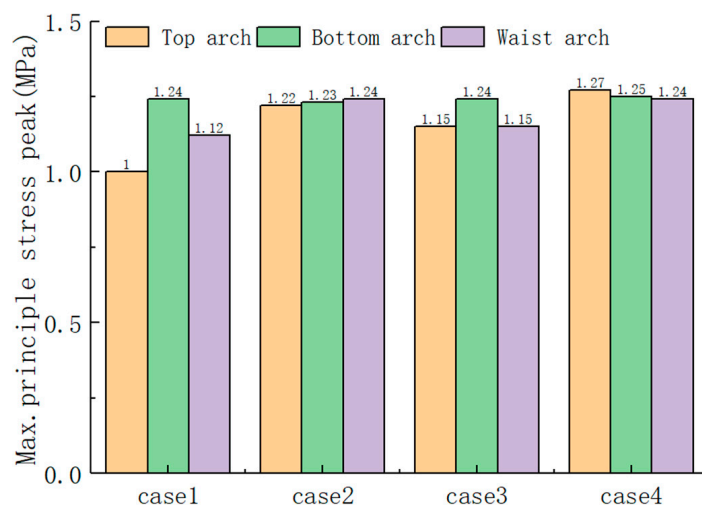


Figure 7. Maximum peak principal stress of monitoring points of lining.

5.2. Lining Structure Displacement Response Analysis

The time course of displacement in the x-direction at the monitoring points of the lining structure under the four working conditions is shown in Figure 8. The displacement-time curves of the top arch, bottom arch, and haunch of the lining under the four working conditions were basically the same, and the wave peaks and troughs appear almost simultaneously, indicating that all parts of the lining were in a synchronous vibration state. The displacement of the lining haunch was greater than that of the top and bottom arches in all four working conditions due to lateral ground vibrations. There was a relatively small difference in relative displacement in the x-direction between the haunch and the top and bottom arches in Condition 1. The difference in relative displacement in the x-direction between the haunch and the top and bottom arches was significantly greater in Conditions 2, 3, and 4 compared to Condition 1, which shows that the contact of the different materials considered exacerbated the seismic displacement response of the lining structure.

The total displacement of the tunnel lining structure monitoring points after the earthquake is shown in Figure 9. The post-earthquake displacement of the haunch was the largest in all four conditions. The post-earthquake displacements of the top arch, bottom arch, and haunch at the monitoring points were 4.28 mm, 5.09 mm, and 5.81 mm, respectively, for Condition 1. Compared to Condition 1, the post-earthquake displacements of the haunches increased by 0.75 mm, 0.05 mm, and 1.68 mm for Conditions 2, 3, and 4, respectively. A comparison of the four scenarios shows that the displacement seismic response of the lining was intensified after the contact between different materials, where the mutual contact between the three materials of the surrounding rock–fault–lining is considered to be the most dangerous.

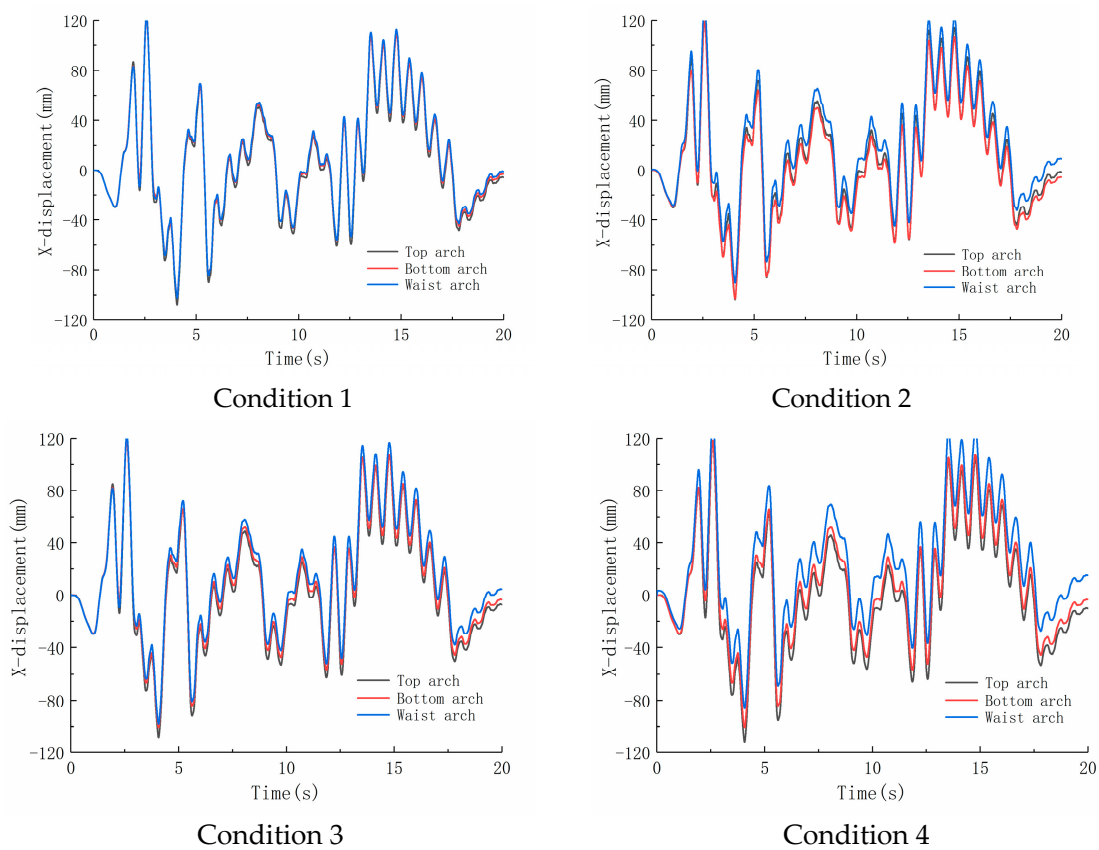


Figure 8. X-displacement–time history of monitoring points of lining.

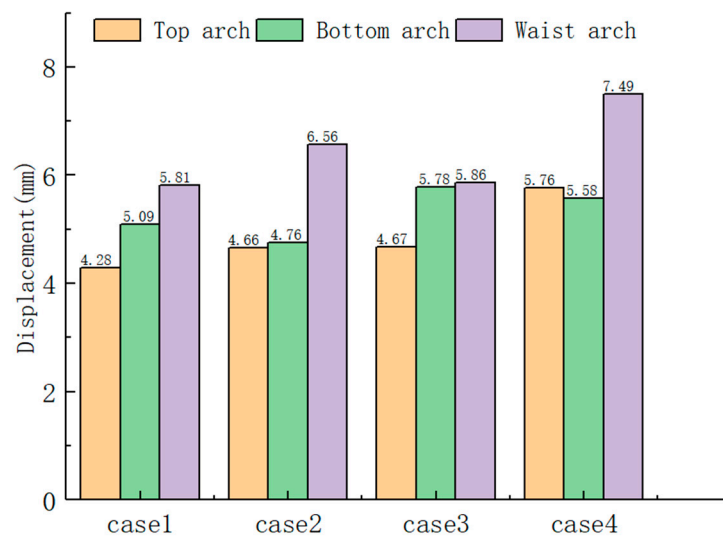


Figure 9. Displacement of monitoring points of lining.

5.3. Security Assessment Analysis

Condition 4, which was the most-risky working condition examined in the previous section, was chosen as the calculation condition. The relative displacement ratios at various PGAs were calculated, and the critical PGA at various monitoring points was solved in accordance with the relative displacement ratio mutation criterion in order to study the maximum peak seismic acceleration that the lining structure could withstand at various monitoring points. The PGA was measured in 0.01 g steps between 0.05 and 0.10 g, 0.05 g steps between 0.1 and 0.6 g, and finally 0.1 g steps up to a maximum PGA of 1.2 g.

Figure 10 depicts the relative displacement ratio against the PGA curve for various lining monitoring points, and was satisfactorily fitted using a 4th-order polynomial fit. The top arch, bottom arch, and haunches were as follows: $R^2 = 0.9989$, $R^2 = 0.9982$, and $R^2 = 0.9999$.

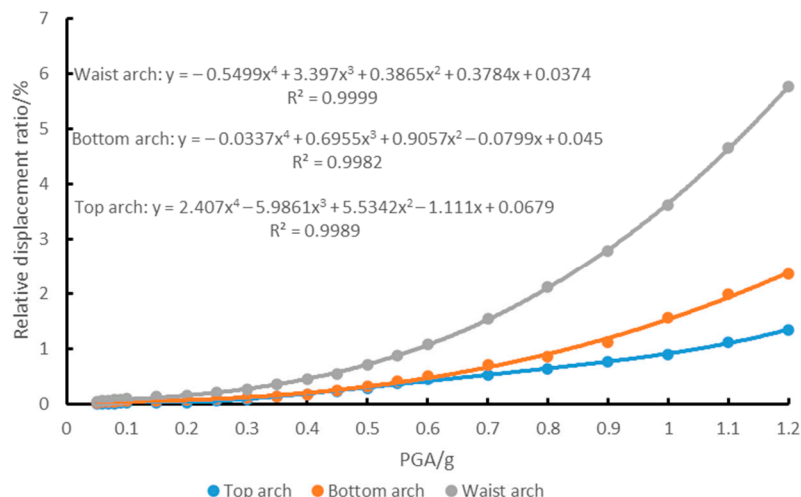


Figure 10. Relative displacement ratio and PGA relationship curve.

Figure 11 depicts the change in the relative displacement ratios and mutation eigenvalues as the PGA changed. For the top arch, when $PGA < 0.35g$ and $D > 0$, the relative displacement ratio was in a steady state of growth. When $0.35 \leq PGA < 0.40$, the value of D became negative and then positive, and it can be judged that the top arch had undergone a mutation according to the mutation condition. When $PGA \geq 0.40g$ and $D > 0$, the relative displacement ratio of the top arch entered another steady state of growth.

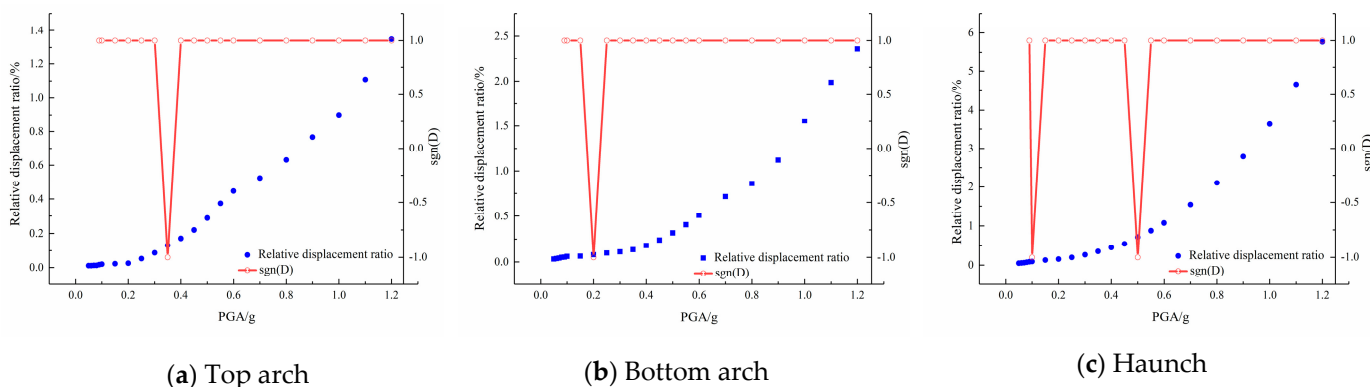


Figure 11. Relative displacement ratio mutation analysis.

For the bottom arch, when $PGA < 0.20g$, $D > 0$, and the relative displacement ratio was in a steady state of growth. When $0.20 \leq PGA < 0.25$, the value of D became negative and then positive, and a mutation in the bottom arch could be judged according to the mutation conditions. When $PGA \geq 0.25g$, $D > 0$, and the relative displacement ratio of the bottom arch entered another steady state of growth.

For the haunch, when $PGA < 0.10g$, $D > 0$, and the relative displacement ratio was in a steady state of growth. When $0.10 \leq PGA < 0.15$, the value of D became negative and then positive, and a mutation in the haunch could be judged according to the mutation conditions. When $0.15 \leq PGA < 0.50$, $D > 0$, indicating that the relative displacement ratio of the haunch had entered another steady state of growth. When $0.50 \leq PGA < 0.55$, the value of D became negative and then positive, and we could tell that the haunch had mutated again according to the mutation conditions. According to the mutation theory, the

maximum peak accelerations when instability occurs in the top and bottom arches of the lining were 0.20 g and 0.35 g, respectively. Two instabilities occurred in the haunch, and the peak accelerations when instability occurred were 0.10 g and 0.50 g.

6. Conclusions

In this study, Lawa Hydropower Station's cross-fault hydraulic tunnels were used as the research object to examine the seismic reaction of these tunnels and evaluate their seismic safety. The following key findings were made:

(1) Four working conditions—no interaction, surrounding rock–lining interaction, surrounding rock–fault interaction, and surrounding rock–lining–fault interaction—were taken into account in a dynamic contact force algorithm that can take into account various medium interactions of surrounding rock–lining–fault. The haunch of the lining structure had larger displacement and stress response values under the transverse seismic load than the top and bottom arches, indicating that it is the weakest component of the lining structure's seismic design. After comparing analyses, it was determined that taking the interaction into account would worsen the lining structure's seismic response in terms of displacement and stress. The perimeter rock–lining–fault interaction condition had the highest displacement and stress response values, making it the most dangerous working condition.

(2) A quantitative technique for evaluating the dynamic instability of hydraulic tunnel lining systems was developed based on the cusp mutation model, employing the relative displacement ratio as the discriminant index. The top arch, bottom arch, and haunch of the lining structure in the fault area could each sustain a maximum peak acceleration of ground vibration of 0.35 g, 0.20 g, and 0.10 g, according to several simulations.

For a more logical seismic safety evaluation of cross-fault hydraulic tunnels, further research is required. Further consideration must be given to ground-shaking characteristics like frequency and duration that affect the seismic response of hydraulic tunnels. Further research is necessary to determine how the tunnel construction responds seismically to various forms of ground shaking, including near-fault impulse-type ground motion and far-field motion.

Author Contributions: Conceptualization, Q.Y. and M.X.; methodology, Q.Y.; software, Q.Y., C.K. and K.W.; validation, Q.Y., C.K. and K.W.; formal analysis, Q.Y.; investigation, Q.Y.; resources, Q.Y.; data curation, C.K.; writing—original draft preparation, K.W.; writing—review and editing, Q.Y.; visualization, Q.Y.; supervision, Q.Y.; project administration, M.X.; funding acquisition, M.X. All authors have read and agreed to the published version of the manuscript.

Funding: This work was financially supported by the National Natural Science Foundation of China (Grant No. 52079097). The supports are greatly acknowledged and appreciated.

Data Availability Statement: The data presented in this study are available on request from the corresponding author.

Acknowledgments: We are grateful to anonymous reviewers for their constructive comments.

Conflicts of Interest: The authors declare no conflict of interest. The funders had no role in the design of the study; in the collection, analyses, or interpretation of data; in the writing of the manuscript; or in the decision to publish the results.

References

1. Amorosi, A.; Boldini, D. Numerical Modelling of the Transverse Dynamic Behaviour of Circular Tunnels in Clayey Soils. *Soil Dyn. Earthq. Eng.* **2009**, *29*, 1059–1072. [[CrossRef](#)]
2. Hashash, Y.M.A.; Hook, J.J.; Schmidt, B.; Yao, J.I.C. Seismic Design and Analysis of Underground Structures. *Tunn. Undergr. Space Technol.* **2001**, *16*, 247–293. [[CrossRef](#)]
3. Wang, Z.; Gao, B.; Jiang, Y.; Yuan, S. Investigation and Assessment on Mountain Tunnels and Geotechnical Damage after the Wenchuan Earthquake. *Sci. China Ser. E-Technol. Sci.* **2009**, *52*, 546–558. [[CrossRef](#)]
4. Dowding, C.H.; Rozan, A. Damage to rock tunnels from earthquake shaking. *J. Geotech. Eng. Div.* **1978**, *104*, 175–191. [[CrossRef](#)]
5. Yoshikawa, K.; Fukuchi, G. Earthquake damage to railway tunnels in Japan. *Adv. Tunn. Technol. Subsurf. Use* **1984**, *4*, 75–83.

6. Sharma, S.; Judd, W.R. Underground opening damage from earthquakes. *Eng. Geol.* **1991**, *30*, 263–276. [[CrossRef](#)]
7. Yoshida, N. Damage to subway station during the 1995 hyogokennambu (kobe) earthquake. In *Earthquake Geotechnical Case Histories for Performance-Based Design*; CRC Press: Boca Raton, FL, USA, 2009; pp. 373–389.
8. Owen, G.N.; Scholl, R.E. *Earthquake Engineering of Large Underground Structures*; Federal Highway Administration and National Science Foundation: Washington, DC, USA, 1981.
9. Yang, Z.; Lan, H.; Zhang, Y.; Gao, X.; Li, L. Nonlinear Dynamic Failure Process of Tunnel-Fault System in Response to Strong Seismic Event. *J. Asian Earth Sci.* **2013**, *64*, 125–135. [[CrossRef](#)]
10. Yu, H.; Chen, J.; Bobet, A.; Yuan, Y. Damage Observation and Assessment of the Longxi Tunnel during the Wenchuan Earthquake. *Tunn. Undergr. Space Technol.* **2016**, *54*, 102–116. [[CrossRef](#)]
11. Huang, J.; Zhao, M.; Du, X. Non-Linear Seismic Responses of Tunnels within Normal Fault Ground under Obliquely Incident P Waves. *Tunn. Undergr. Space Technol.* **2017**, *61*, 26–39. [[CrossRef](#)]
12. Geng, P.; Wu, C.; Tang, J.; Li, L. Analysis of Dynamic Response Properties for Tunnel Through Fault Fracture Zone. *Chin. J. Rock Mech. Eng.* **2012**, *31*, 1406–1413.
13. Peng, S.; Zeng, Y.; Fan, L.; Wang, G.; Xun, Z.; Chen, G. Numerical Investigation on the Dynamic Response of Fault-Crossing Tunnels under Strike-Slip Fault Creep-Slip and Subsequent Seismic Shaking. *Buildings* **2023**, *13*, 1163. [[CrossRef](#)]
14. Chen, H.; Gao, M.; Wang, W.; Liu, Q.; Lu, T.; Peng, G. Study on the deformation law and damage mechanism of cross fault tunnel lining. *Adv. Eng. Sci.* **2018**, *50*, 38–46.
15. Li, L.; He, C.; Geng, P.; Cao, D. Analysis of Seismic Dynamic Responses of Tunnel through Fault Zone in High Earthquake Intensity Area. *J. Chongqing Univ.* **2012**, *35*, 92–98.
16. Wang, X.; Xiong, Q.; Zhou, H.; Chen, J.; Xiao, M. Three-Dimensional (3D) Dynamic Finite Element Modeling of the Effects of a Geological Fault on the Seismic Response of Underground Caverns. *Tunn. Undergr. Space Technol.* **2020**, *96*, 103210. [[CrossRef](#)]
17. Liu, G.; Xiao, M.; Yang, Y.; Ren, J. Numerical Simulation and Analysis Method of Seismic Response for Hydraulic Tunnel across Fault. *J. Hunan Univ.* **2018**, *45*, 140–148.
18. Liu, G.; Zhang, Y.; Ren, J.; Xiao, M. Seismic Response Analysis of Tunnel through Fault Considering Dynamic Interaction between Rock Mass and Fault. *Energies* **2021**, *14*, 6700. [[CrossRef](#)]
19. Shahidi, A.R.; Vafaeian, M. Analysis of Longitudinal Profile of the Tunnels in the Active Faulted Zone and Designing the Flexible Lining (for Koohrang-III Tunnel). *Tunn. Undergr. Space Technol.* **2005**, *20*, 213–221. [[CrossRef](#)]
20. Liu, S.; Liu, S.; Lu, S.; Ma, F.; Pei, G. Seismic Behaviour of Shallow Tunnelling Method Tunnels Accounting for Primary Lining Effects. *Buildings* **2023**, *13*, 20. [[CrossRef](#)]
21. Zlatanovic, E.; Lukic, D.C.; Prolovic, V.; Bonic, Z.; Davidovic, N. Comparative Study on Earthquake-Induced Soil-Tunnel Structure Interaction Effects under Good and Poor Soil Conditions. *Eur. J. Environ. Civ. Eng.* **2015**, *19*, 1000–1014. [[CrossRef](#)]
22. Wang, X.; Chen, J.; Zhang, Y.; Xiao, M. Seismic Responses and Damage Mechanisms of the Structure in the Portal Section of a Hydraulic Tunnel in Rock. *Soil Dyn. Earthq. Eng.* **2019**, *123*, 205–216. [[CrossRef](#)]
23. Liu, G.; Xiao, M.; Chen, J.; Chen, S. Numerical simulation of seismic response for tunnel portal section in strong earthquake area. *J. Cent. S. Univ.* **2018**, *49*, 2804–2812.
24. Liu, G.; Xiao, M.; Chen, J. Effect of Seismic Parameters on the Safety Factor for an Underground Carven. *Mod. Tunn. Technol.* **2018**, *55*, 98–105.
25. Prasad, J.; Kumar, J. Seismic stability of a long unsupported circular tunnel. *Comput. Geotech.* **2012**, *44*, 109–115.
26. Chakraborty, D.; Kumar, J. Stability of a long unsupported circular tunnel in soils with seismic forces. *Nat. Hazards* **2013**, *68*, 419–431. [[CrossRef](#)]
27. Liu, Y.; Wu, Z.; Yang, Q.; Leng, K. Dynamic stability evaluation of underground tunnels based on deformation reinforcement theory. *Adv. Eng. Softw.* **2018**, *124*, 97–108. [[CrossRef](#)]
28. Cheng, X.; Li, X.; Fan, J.; Li, G. Seismic Stability of a tunnel considering the dynamic geologic parameters of loess. *Geotech. Geol. Eng.* **2018**, *36*, 3583–3600. [[CrossRef](#)]
29. Zhou, Z.; Chen, Z.; Zhang, L.; Nian, G.; Wang, J.; Jiao, X. Energy principle based catastrophe study of slope stability in open-pit excavation. *Rock Soil Mech.* **2019**, *40*, 4881–4889.
30. Liu, J.; Qin, S.; Zhang, Z. Study on catastrophic model with cusp point for failure of rock mass with a gentle inclination. *Chin. J. Geotech. Eng.* **2001**, *23*, 42–44.
31. Tao, Y.; Cao, J.; Hu, J.; Dai, Z. A Cusp Catastrophe Model of Mid-Long-Term Landslide Evolution over Low Latitude Highlands of China. *Geomorphology* **2013**, *187*, 80–85. [[CrossRef](#)]
32. Qiao, C.; Guo, Y.; Li, C. Study on Rock Burst Prediction of Deep Buried Tunnel Based on Cusp Catastrophe Theory. *Geotech Geol. Eng.* **2021**, *39*, 1101–1115. [[CrossRef](#)]
33. Xu, Z.; Xu, X.; Tang, C. Theoretical analysis of a cusp catastrophe bump of coal pillar under hard rocks. *J. China Coal Soc.* **1995**, *20*, 485–491.
34. Xue, Y.; Wang, D.; Li, S.; Qiu, D.; Li, Z.; Zhu, J. A Risk Prediction Method for Water or Mud Inrush from Water-Bearing Faults in Subsea Tunnel Based on Cusp Catastrophe Model. *KSCE J. Civ. Eng.* **2017**, *21*, 2607–2614. [[CrossRef](#)]
35. Peng, Y.; Wu, L.; Chen, C.; Yue, J. Stability Analysis of Surrounding Rock in Tunnel Crossing Water-Rich Fault Based on Catastrophe Theory. *Geotech. Geol. Eng.* **2020**, *38*, 415–423. [[CrossRef](#)]

36. Du, W.; Sheng, Q.; Fu, X.; Tang, H.; Chen, H.; Du, Y.; Zhou, Y. Dynamic Stability Analysis and Failure Mechanism of Yanyang Village Landslide under Earthquake. *Rock Soil Mech.* **2020**, *41*, 2461–2469.
37. Shu, L.; Jingbo, L.; Jiaguang, S.; Yujian, C. A Method for Analyzing Three-Dimensional Dynamic Contact Problems in Visco-Elastic Media with Kinetic and Static Friction. *Comput. Struct.* **2003**, *81*, 2383–2394. [[CrossRef](#)]
38. Wang, X.; Chen, J.; Xiao, M.; Wu, D. Seismic Response Analysis of Concrete Lining Structure in Large Underground Powerhouse. *Math. Probl. Eng.* **2017**, *2017*, 1–14. [[CrossRef](#)]
39. Wang, X.; Chen, J.; Xiao, M. Seismic Responses of an Underground Powerhouse Structure Subjected to Oblique Incidence SV and P Waves. *Soil Dyn. Earthq. Eng.* **2019**, *119*, 130–143. [[CrossRef](#)]
40. Zhao, J.; Xiao, M.; Chen, J.; Li, D. Simulation Methodology of Weak Structural Planes in Large Underground Chamber Based on Element Reconstruction and Node Separation. *J. Hunan Univ.* **2017**, *44*, 134–142.
41. Zeeman, E.C. *Catastrophe Theory: Selected Papers, 1972–1977*; Addison-Wesley Publishing Company: Oxford, UK, 1977.
42. Ma, Z.; Zhang, W.; Zhou, Q.; Tang, K. A deformation-based method for seismic fragility analysis of gravity dam. *J. Vib. Shock.* **2017**, *36*, 51–58.
43. Zhang, Z.; Xiao, M.; Chen, J. Simulation of earthquake disaster process of large-scale underground caverns using three-dimensional dynamic finite element method. *Chin. J. Rock Mech. Eng.* **2011**, *30*, 509–523.

Disclaimer/Publisher’s Note: The statements, opinions and data contained in all publications are solely those of the individual author(s) and contributor(s) and not of MDPI and/or the editor(s). MDPI and/or the editor(s) disclaim responsibility for any injury to people or property resulting from any ideas, methods, instructions or products referred to in the content.